Comparative Analysis of the 2020 November 29 Solar Energetic Particle Event Observed by Parker Solar Probe

D. Lario[1] , I. G. Richardson[1,2] , E. Palmerio[3,4] , N. Lugaz[5] , S. D. Bale[3,6,7,8] , M. L. Stevens[9] , C. M. S. Cohen[10] ,
J. Giacalone[11] , D. G. Mitchell[12] , A. Szabo[1] , T. Nieves-Chinchilla[1] , L. B. Wilson, III[1] , E. R. Christian[1] ,
M. E. Hill[12] , D. J. McComas[13] , R. L. McNutt, Jr.[12] , N. A. Schwadron[5,13] , and M. E. Wiedenbeck[14]

[1] Heliophysics Division, NASA Goddard Space Flight Center, Greenbelt, MD 20771, USA; david.larioloyo@nasa.gov
[2] Department of Astronomy, University of Maryland, College Park, MD 20742, USA
[3] Space Sciences Laboratory, University of California at Berkeley, Berkeley, CA 94720, USA
[4] CPAESS, University Corporation for Atmospheric Research, Boulder, CO 80301, USA
[5] Institute for the Study of Earth, Oceans, and Space, Department of Physics, University of New Hampshire, Durham, NH 03824, USA
[6] Physics Department, University of California at Berkeley, Berkeley, CA 94720, USA
[7] The Blackett Laboratory, Imperial College London, London, SW7 2AZ, UK
[8] School of Physics and Astronomy, Queen Mary University of London, London, E1 4NS, UK
[9] Center for Astrophysics—Harvard & Smithsonian, Cambridge, MA 02138, USA
[10] California Institute of Technology, Pasadena, CA 91125, USA
[11] Lunar & Planetary Laboratory, University of Arizona, Tucson, AZ 85721, USA
[12] The Johns Hopkins University, Applied Physics Laboratory, Laurel, MD 20723, USA
[13] Department of Astrophysical Sciences, Princeton University, Princeton, NJ 08544, USA
[14] Jet Propulsion Laboratory, California Institute of Technology, Pasadena, CA 91109, USA

Abstract

We analyze two specific features of the intense solar energetic particle (SEP) event observed by Parker Solar Probe (PSP) between 2020 November 29 and 2020 December 2. The interplanetary counterpart of the coronal mass ejection (CME) on 2020 November 29 that generated the SEP event (hereafter ICME-2) arrived at PSP (located at 0.8 au from the Sun) on 2020 December 1. ICME-2 was preceded by the passage of an interplanetary shock at 18:35 UT on 2020 November 30 (hereafter S2), that in turn was preceded by another ICME (i.e., ICME-1) observed in situ on 2020 November 30. The two interesting features of this SEP event at PSP are the following: First, the presence of the intervening ICME-1 affected the evolution of the $\lesssim 8$ MeV proton intensity-time profiles resulting in the observation of inverted energy spectra throughout the passage of ICME-1. Second, the sheath region preceding ICME-2 was characterized by weak magnetic fields compared to those measured immediately after the passage of the shock S2 and during the passage of ICME-2. Comparison with prior SEP events measured at 1 au but with similar characteristics indicates that (1) low-energy particles accelerated by S2 were excluded from propagating throughout ICME-1, and (2) the low magnetic fields measured in the sheath of ICME-2 resulted from the properties of the upstream solar wind encountered by ICME-2 that was propagated into the sheath, whereas the energy density of the high-energy particles in the sheath did not play a dominant role in the formation of these low magnetic fields.

Unified Astronomy Thesaurus concepts: Solar energetic particles (1491); Interplanetary shocks (829); Solar coronal mass ejections (310); Interplanetary magnetic fields (824)

1. Introduction

Large solar energetic particle (SEP) events are typically associated with shock waves driven away from the Sun by coronal mass ejections (CMEs; e.g., Kahler et al. 1984). As a CME propagates and expands in interplanetary (IP) space, the ambient solar wind plasma piles up in front of the CME, forming a sheath-like region (e.g., Siscoe & Odstrcil 2008). Fast CMEs, whose speed relative to the solar wind exceeds the magnetosonic speed, generate fast forward shocks ahead of them, compressing the upstream solar wind (Hundhausen 1972). The IP manifestation of a CME, also known as an interplanetary coronal mass ejection (ICME), generally includes a magnetically dominated plasma region, known as the *magnetic ejecta* (ME), that is usually preceded by a dense sheath and occasionally by a fast forward shock at the leading edge (e.g., Lugaz et al. 2018). An ICME whose leading edge propagates faster than the preceding solar wind, but not fast enough to drive a shock, deflects and compresses the upstream plasma flow, forming a disturbed sheath-like region with a fast magnetosonic wave at the leading edge that may not

have steepened into a fully developed shock (e.g., Liu et al. 2006; Kilpua et al. 2017). Sheath regions are typically characterized by increased solar wind density and temperature together with an enhanced magnetic field that fluctuates in intensity and direction, whereas the ME is typically characterized by in situ signatures that differ from those in the ambient solar wind such as a smoothly rotating field, low plasma β (defined as the ratio of the plasma pressure to the magnetic pressure), low solar wind proton temperature, presence of bidirectional suprathermal electrons, enhanced ion abundances with elevated charge states, and a linearly decreasing speed profile, indicative of expansion (e.g., Zurbuchen & Richardson 2006, and references therein). Not all ICME signatures appear in every single ICME, and when they appear they are not often synchronized (Neugebauer & Goldstein 1997; Richardson & Cane 2010a), presumably because they arise from different physical processes occurring near the Sun or during propagation of the ICME (Zurbuchen & Richardson 2006). In this paper, we will use the term ICME to identify the ME, while the sheath region ahead of the ME and the IP shock will be treated as separate entities, noting however, that some recent authors consider

"ICME" to refer to the shock, sheath, and ME together (e.g., Salman et al. 2020; Temmer et al. 2021).

Strong IP shocks ahead of fast ICMEs may be efficient accelerators of low-energy ($\lesssim 20\,\mathrm{MeV}$) ions when arriving at 1 au (e.g., Bavassano-Cattaneo et al. 1986; Giacalone 2015, and references therein). Energetic particle intensity enhancements associated with the passage of IP shocks have been historically referred to as *energetic storm particle* (ESP) events because of their frequent association with geomagnetic storms (Bryant et al. 1962). ESP events show a wide variety of energy spectra and intensity-time profiles (e.g., van Nes et al. 1984; Lario et al. 2003). A particular type of particle enhancement, showing an intensity that exponentially increases ahead of the shock, maximizes at the time of the shock passage and remains approximately constant downstream of the shock, is consistent with the predictions of the diffusive shock acceleration (DSA) theory developed by Lee (1983) (see also Gordon et al. 1999). However, agreement between theoretical predictions and observations is rarely found (Kennel et al. 1986; Lario et al. 2005; Desai et al. 2012), although there is better agreement when considering only strong shocks (Giacalone 2012). In the case of fast ICMEs, the sheath formed between the shock and the leading edge of the ICME may include structures such as planar and rotational discontinuities, mini-flux ropes, and magnetic islands (e.g., Kataoka et al. 2005; Palmerio et al. 2016; Shaikh et al. 2018; Moissard et al. 2019) that have been suggested to play significant roles in particle acceleration (e.g., Zhao et al. 2018) and transport (e.g., Sanderson et al. 2000). In intense ESP events, enhanced energetic particle intensities may have an effect on the plasma and magnetic field observed upstream of the IP shock (Lario & Decker 2002; Russell et al. 2013; Lario et al. 2015a, 2015b), similar to the foreshock diamagnetic cavities found upstream of the Earth's bow shock (Sibeck et al. 2001). The formation of these cavities is attributed to the effect of ions reflected from the bow shock that, via beam instabilities, generate waves that scatter and isotropize the reflected ion beams, producing an increase in the thermal pressure that creates an overpressure compared to surrounding regions not connected to the bow shock. Subsequent filling by shock-accelerated particles provides the additional pressure to expand these cavities and hence decrease the density and magnetic field strength (see Sibeck et al. 2002, and references therein).

After the passage of the shock and the sheath region, the entry of the spacecraft into the ICME is usually accompanied by a depression of the energetic particle intensities with respect to the intensities measured at the time of the IP shock passage and throughout the sheath region (e.g., Sanderson et al. 1990; Kahler & Reames 1991; Cane et al. 1993; Richardson & Cane 2011). This suggests that, under the assumption that ICMEs are isolated magnetic structures, the access of shock-accelerated particles into the ICME is limited. Energetic particles can penetrate into the ICME primarily through cross-field diffusion and/or drift processes (Cane et al. 1995). The larger Larmor radius and speed of high-energy particles leads to a more efficient penetration of these particles within the ICME than the lower energy particles that are more easily excluded from the ICME (Laitinen & Dalla 2021). The decrease of particle intensity is determined then by the size, geometry, and gradient scale lengths of the region in which the field lines in the ICME are isolated from the external regions as well as the scattering conditions undergone by the particles around the ICME (Laitinen & Dalla 2021).

In this paper, we analyze two peculiarities observed by Parker Solar Probe (PSP; Fox et al. 2016) during the first widespread SEP event of solar cycle 25 (Kollhoff et al. 2021). This SEP event originated when a fast CME, associated with an M4.4 class X-ray flare with onset at 12:34 UT on 2020 November 29 (day of year 334) from NOAA active region (AR) 12790 at S23E99 occurred (Chitta et al. 2021). According to the CME catalog of the Coordinated Data Analyses Web (CDAW; Yashiro et al. 2004)[15] based on images from the Large Angle and Spectrometric Coronagraph (LASCO; Brueckner et al. 1995) on board the Solar and Heliospheric Observatory (SOHO; Domingo et al. 1995), this CME propagated with a plane-of-sky speed of $2077\,\mathrm{km\,s^{-1}}$ (measured at the position angle PA = 94°, where PA is measured counterclockwise from solar north). At that time, PSP was located at 0.80 au from the Sun and 96° eastward of Earth in longitude. Therefore, the flare and CME originated from a region very close to the central meridian seen from PSP. As expected, the IP counterpart of this CME (henceforth ICME-2) arrived at PSP on 2020 December 1 (day of year 336), preceded by the passage of an IP shock at 18:35 UT on 2020 November 30 (henceforth S2). An overview of the energetic particle observations by the Integrated Science Investigation of the Sun (IS☉IS; McComas et al. 2016) on board PSP has been presented by Cohen et al. (2021), whereas detailed observations of the SEP event by the multiple spacecraft distributed at heliocentric distances $\lesssim 1$ au have been described by Kollhoff et al. (2021).

The two peculiarities of this SEP event analyzed here are [1] the impact on the SEP event of the passage by PSP of an ICME (henceforth ICME-1) that preceded shock S2, and [2] the sheath region of ICME-2 that was characterized by a low magnetic field magnitude compared to the fields measured immediately after the passage of S2 and during the passage of ICME-2. We compare the properties of this SEP event at PSP with prior events with similar characteristics observed at 1 au, and in the light of these earlier events, discuss both the effects of ICME-1 on the development of the SEP event observed by PSP, and whether the weak magnetic fields in the sheath region of ICME-2 could be accounted for by a high energetic particle energy density. Section 2 describes the observations of the 2020 November 29 SEP event by PSP. The evolution of the particle intensities in similar SEP events preceded by intervening ICMEs is described in Section 3, paying special attention to the well-studied SEP event that occurred on 2000 July 14 (often known as the *Bastille Day* event), which had a number of similarities with the 2020 November 29 event at PSP. In Section 4, we compare SEP events associated with IP shocks with downstream magnetic field profiles similar to that in the ICME-2 sheath and discuss the possible effect of the energy density of shock-accelerated particles on the sheath magnetic fields. In Section 5 we discuss the main results of the comparative analyses and Section 6 summarizes the main conclusions of this work.

2. PSP Observations

We use in situ measurements of plasma, magnetic field, and energetic particles at PSP collected by the Solar Wind

---

[15] cdaw.gsfc.nasa.gov/CME _ list/.

Electrons Alphas and Protons (SWEAP) experiment (Kasper et al. 2016), the fluxgate magnetometers of the FIELDS suite of instruments (Bale et al. 2016), and the energetic particle instruments of the Integrated Science Investigation of the Sun (IS⊙IS; McComas et al. 2016). In particular, we use data from the Solar Probe Cup (SPC) of SWEAP, which measures the solar wind proton temperature, density, and velocity (Case et al. 2020). IS⊙IS consists of a suite of two energetic particle instruments: (1) EPI-Lo, which measures particles using the time-of-flight versus energy technique and determines the composition, spectra, and anisotropies of particles with energies from $\sim$20 keV nucleon^{-1} to several MeV nucleon^{-1} (Hill et al. 2017), and (2) EPI-Hi, which uses the dE/dx versus residual energy technique to measure particles over the energy range of $\sim$1–200 MeV nucleon^{-1} (Wiedenbeck et al. 2017). The EPI-Hi telescopes employ a system of dynamic thresholds designed to measure elevated particle intensities (McComas et al. 2016). During the SEP event on 2020 November 29, intensities were high enough to trigger the pre-established intensity thresholds at different energies. The EPI-Hi particle intensities displayed in this paper have been corrected for changes in the geometric factors that resulted from the varying energy thresholds of the instrument during this period (see details in Cohen et al. 2021).

Figure 1 shows, from top to bottom, (a) proton intensities measured by the triple coincidence data system (ChanR) of EPI-Lo (Hill et al. 2017) averaged over all the apertures of the instrument (except for the apertures 3 and 10 blocked by EPI-Hi, 11 and 12 due to partial effects of the EPI-Hi blockage, 31 noisy due to dust penetration, and 51 and 52 due to noisy counts), and the average of the intensities obtained from the sides A and B of the double-ended High-Energy Telescope (HET; Wiedenbeck et al. 2017) of EPI-Hi; (b) the average of the electron count rates measured in the wedges 3 and 7 of EPI-Lo (red trace) and in sides A and B of HET (black trace); solar wind proton (c) speed, (d) density, and (e) temperature as obtained from SPC measurements; and magnetic field (f) magnitude, (g) elevation angle, and (h) azimuth angle in the spacecraft-centered Radial–Tangential–Normal (RTN) coordinate system as measured by FIELDS.

During the time interval covered in Figure 1, PSP was slewed such that the SPC instrument was pointed 45° off of the Sun–spacecraft line. The spacecraft also executed 180° conical rolls about the Sun–spacecraft line at varying intervals 2–3 times per day. With this orientation, the solar wind was outside of the 30° nominal (Sun-pointed) SPC field of view. The nominal field of view for SPC is defined as the cone for which flux may be detected simultaneously upon all four quadrants of the sensor (Case et al. 2020), enabling determination of the vector flow direction and the geometric factor required for calculation of the absolute proton density. While at least two of the four SPC sensor plates measured zero flux, a significant proton signal was often measured at the other two plates during part of 2020 November 29 and 30. In order to estimate the solar wind speed, temperature, and density, the SPC charge flux distributions from the plates with signals were grouped into 5 minute segments and fit using the SPC Maxwellian response function under the ad hoc constraint that the flow was purely parallel to the RTN radial direction. This constraint and the resulting solar wind speed estimates (Figure 1(c)) were corroborated to within $\pm$ 50 km s^{-1} by observing the apparent change in speed, in the spacecraft frame, across each conical roll maneuver. The proton density estimate (Figure 1(d)) was compared with observations from the FIELDS Radio Frequency Spectrometer (RFS) Low Frequency Receiver (Moncuquet et al. 2020), which resolved density-sensitive electron plasma frequency oscillations for an extended period on 2020 November 29–December 1, showing a good corroboration of the peak density within $\sim$10%. Finally, the temperature estimates shown in Figure 1(e) are derived from the Z_{SC} diagonal component of the proton pressure tensor only, where Z_{SC} is the spacecraft axis perpendicular to the heat shield of the spacecraft that coincides with the symmetry axis of the SPC field of view and that nominally points toward the Sun except during specific spacecraft maneuvers (Guo et al. 2021) such as those performed during the period under analysis. This quantity is equal to the scalar temperature, i.e., $T_p = T_{Z,SC}$ when the proton phase space distribution is isotropic. The assumption that $T_p \approx T_{Z,SC}$ is typically good to within $\sim$25%–50% in the solar wind. Finally, we note that the SPC measurements under this unusual circumstance are frequently noise-limited. This means that the probability of detecting and measuring the solar wind proton peak is not consistent, but correlated with the proton density (peak magnitude) and anticorrelated with the temperature (peak width). The subset of measurements that have been successfully reconstructed here may thus be assumed to be colder and denser, on average, than a complete solar wind sample would be.

The red arrows in Figure 1 indicate the occurrence of the M4.4 flare temporally associated with the origin of the SEP event. The solid vertical lines S1 and S2 in Figure 1 indicate the passage of possible IP shocks at 23:07 UT on day 334 and at 18:35 UT on day 335, respectively. The identification of the shock passages is based exclusively on the observation of discontinuous increases in the magnetic field magnitude. The lack of accurate plasma measurements does not allow a precise determination of whether these magnetic field increases correspond to actual shock passages. The gray vertical bars indicate the passage of two ICMEs (ICME-1 from 03:07 UT to 15:56 UT on day 335, and ICME-2 from 02:24 UT to 11:45 UT on day 336) as identified by smooth magnetic field evolution with hints of coherent field rotation (T. Nieves-Chinchilla et al. 2021, in preparation). Similarly to the IP shock identification, the lack of appropriate plasma measurements does not allow a more complete assessment of the signatures usually observed during the passage of ICMEs (e.g., Zurbuchen & Richardson 2006), although a depression of the solar wind proton temperature seems to be observed during the passage of ICME-1 (Figure 1(e)).

The most likely solar origin of ICME-1 is a CME observed by LASCO/C2 at 21:12 UT on day 331 from AR 12787 at N32E89 with a plane-of-sky speed 572 km s^{-1} as reported in the CDAW CME catalog. Extreme ultraviolet (EUV) images from the Extreme Ultraviolet Imager (EUVI; Wuelser et al. 2004) on board the spacecraft A of the Solar Terrestrial Relations Observatory (STEREO-A; Kaiser et al. 2008) detected an EUV wave with onset at $\sim$20:30 UT on day 331 most likely associated with the origin of the CME. The average transit speed of the ICME-1 leading edge to travel from the Sun to PSP is about $\sim$426 km s^{-1}, whereas that of the preceding shock (indicated by S1 in Figure 1) is $\sim$449 km s^{-1}. In comparison, considering the onset of the M4.4 flare as origin of the ICME-2 on the Sun, we infer an average transit speed for the shock S2 to travel from the Sun to PSP of $\sim$1114 km s^{-1}
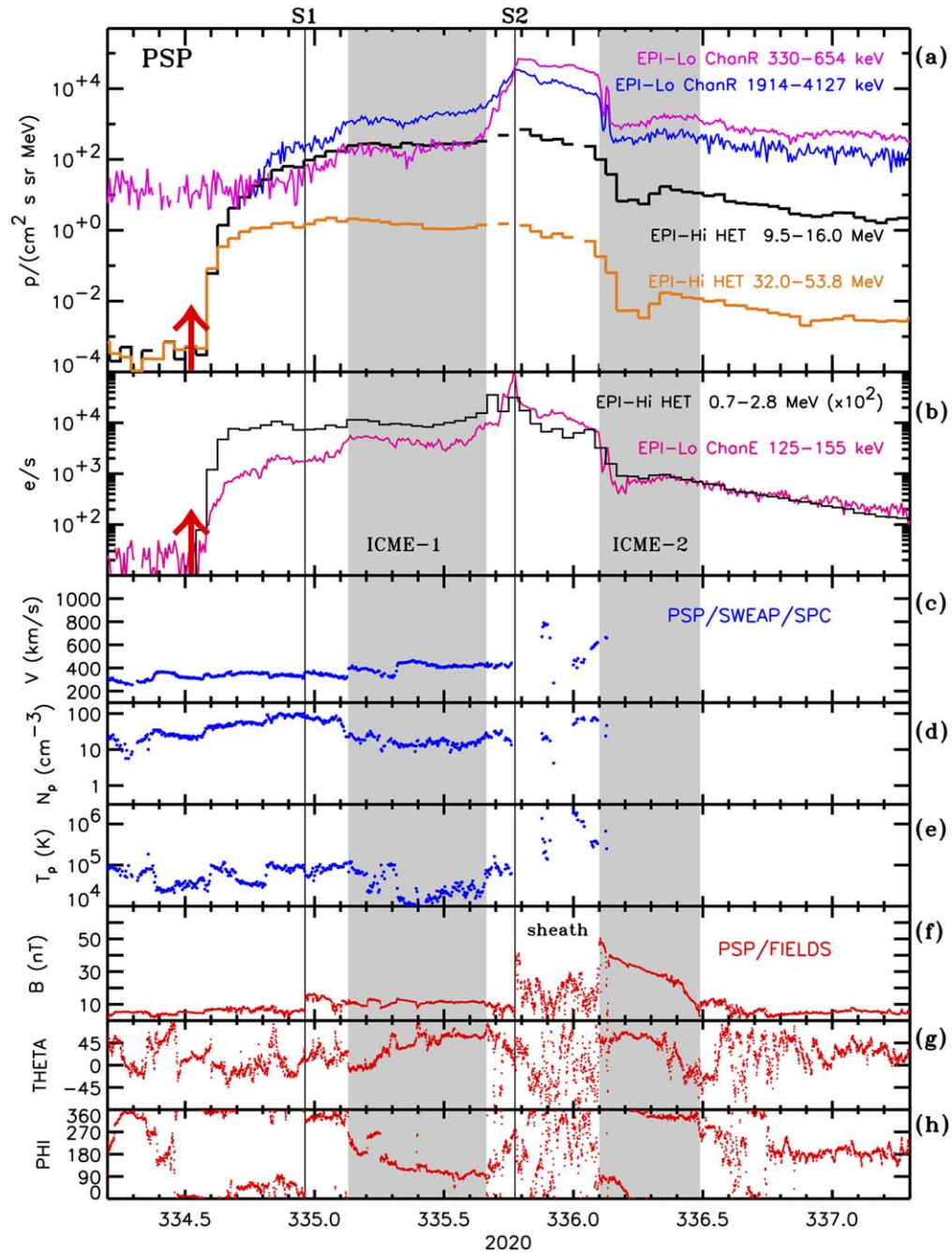
Figure 1. From top to bottom: (a) 10 minute averages of the proton intensities observed by the triple coincidence system (ChanR) of EPI-Lo (two top traces) and averages of the hourly proton intensities measured by the sides A and B of EPI-Hi HET (black and orange traces); (b) 10 minute averages of the electron counting rates observed by the wedges 3 and 7 of EPI-Lo (red line) and average of the hourly electron rates measured by the sides A and B of EPI-Hi/HET (red trace); proton solar wind (c) speed, (d) density, and (e) temperature recovered from SWEAP/SPC measurements; and magnetic field (f) magnitude, (g) elevation angle, and (h) azimuth angle in RTN coordinates as measured by FIELDS. The solid vertical lines identify the possible passages of shocks. The gray shaded bands identify the passage of ICME-1 and ICME-2. The red arrows in (a) and (b) indicate the onset of the M4.4 solar flare temporally associated with the origin of the SEP event. Data gaps in the EPI-Hi/HET curves in (a) and (b) correspond to intervals when EPI-Hi/HET changed between different thresholds.

and for the leading edge of ICME-2 of $\sim 883\,\mathrm{km\,s^{-1}}$. Possible interactions between ICME-1 and ICME-2 during their transit from the Sun to PSP are analyzed by T. Nieves-Chinchilla (2021, in preparation) and Palmerio E. et al. (2021, in preparation).

The onset of the SEP event at PSP occurred shortly after the occurrence of the M4.4 flare indicated by red arrows in Figures 1(a) and (b). We note that the passage of shock S1 was not associated with a significant change in the low-energy

($\lesssim 20\,\mathrm{MeV}$) proton intensity-time profiles that were still increasing. A few minutes prior to the entry of the spacecraft into ICME-1, proton intensities at energies between $\sim 221\,\mathrm{keV}$ and $\sim 20\,\mathrm{MeV}$ increased, whereas proton intensities at higher energies remained constant or slightly decreased throughout the passage of ICME-1. The electron intensities also increased upon the entry of PSP into ICME-1, with the enhancement being more prominent at lower energies, followed by a slight decline extending into the trailing half of ICME-1.
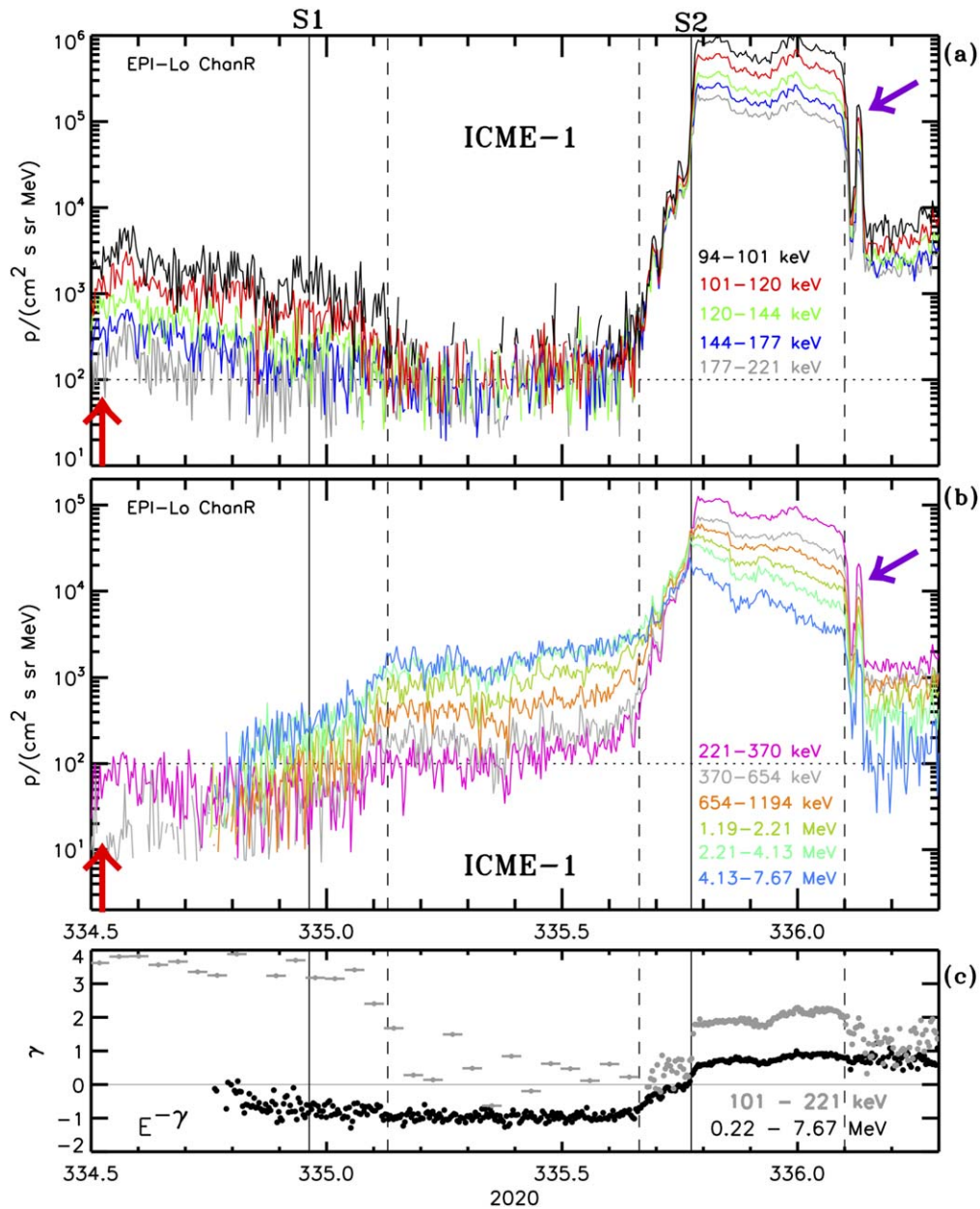
Figure 2. From top to bottom: 5 minute averages of the proton intensities observed at energies at energies (a) from 94 keV to 221 keV and (b) from 221 keV to 7.67 MeV by the triple coincidence system (ChanR) of EPI-Lo; (c) spectral index γ assuming that the differential flux intensities follow a power law $\propto E^{-\gamma}$ for energies 101–221 keV (gray symbols) and 221–7675 keV (black symbols).

2.1. Inverted Particle Energy Spectra Throughout the Passage of ICME-1

A peculiarity of the low-energy proton intensities observed throughout the passage of ICME-1 is the profound change in the proton energy spectrum between ~220 keV and ~8 MeV during the passage of ICME-1 compared with the upstream spectrum. The two top panels of Figure 2 show proton intensities obtained from the EPI-Lo triple coincidence (ChanR) measurements in different energy channels from 94 keV to 7.67 MeV. For clarity purposes we show energy channels below and above 221 keV in Figures 2(a) and 2(b), respectively. Prior to the occurrence of the M4.4 solar flare associated with the SEP event, $\lesssim$300 keV proton intensities were already elevated (as well as the $\lesssim$20 MeV proton intensities measured by the LET telescope of EPI-Hi; not shown here) due to previous events. Proton intensities at energies

$\lesssim$221 keV showed a decrease upon the entry of PSP into ICME-1. In fact, only sporadic individual ChanR counts at energies $\lesssim$221 keV were measured throughout the ICME-1 passage. In contrast, as already mentioned, higher-energy proton intensities increased at the entry into ICME-1 and remained constant or slightly increased throughout ICME-1. The horizontal dotted line in Figures 2(a) and (b) indicates the intensity value 10^2 protons $(\text{cm}^2\,\text{s}\,\text{sr}\,\text{MeV})^{-1}$, showing that throughout ICME-1, the higher the energy of the particles, the higher the measured intensity, resulting in an *inverted* spectrum at energies between 221 keV and 7.67 MeV.

Figure 2(c) shows the spectral index γ obtained by assuming that the energy spectra follow a power law $\propto E^{-\gamma}$ over the energy ranges of 101–221 keV (gray symbols) and 221–7675 keV (black symbols). In order to fit the energy spectra, we have assumed an energy for each channel in the specified energy range given by the

geometric mean energy of the channel and used hourly averages of $\lesssim 221$ keV proton intensities prior to the trailing edge of ICME-1 and 5 minute intensity averages for the rest of the period as well as for energies $\gtrsim 221$ keV. Thus, an unusual feature of this SEP event is the inverted energy spectra (i.e., $\gamma < 0$) observed over the energy range 221 keV–7.67 MeV for a period of more than ~ 21 hr, from the onset of the event up to the passage of the trailing edge of ICME-1. In order to determine the conditions that led to the observation of this inverted spectrum, in Section 3 we analyze similar events associated with the passage of IP shocks with the presence of a preceding ICME.

The exit of PSP from ICME-1 was marked by an increase in $\lesssim 8$ MeV proton intensities in such a way that intensities at different energies were similar, leading to a relatively flat spectrum ($\gamma \sim 0$). Unfortunately, changes in the energy threshold mode used by EPI-Hi occurring close to shock passage (Cohen et al. 2021) resulted in data gaps that do not allow us to see the complete evolution of the high-energy proton intensities before the arrival of S2 (see Figure 1(a)). The low-energy ($\lesssim 8$ MeV) proton intensities peaked with the arrival of the shock S2, which was followed by a period of elevated intensities throughout the sheath region of ICME-2. Detailed analyses of the particle and magnetic field observations in the vicinity of shock S2 are presented in Giacalone et al. (2021). The entry of PSP into ICME-2 was accompanied by a drastic depletion of particle intensities at all energies as is usually observed upon the entry of spacecraft into ICMEs (e.g., Cane & Lario 2006). Interestingly, the low intensities within ICME-2 were interrupted by a ~ 30-minute interval with enhanced particle intensities (clearly seen at the higher-time resolution of EPI-Lo data as indicated by the purple arrow in Figure 2(a) and 2(b)). This short-lived particle increase coincided with a depression in the magnetic field intensity (evident from close inspection of Figure 1(f)), suggesting that either PSP briefly exited ICME-2 or that magnetic reconnection occurred at the leading edge of ICME-2 resulting in open field lines, and thus the observation of particles with a similar energy spectrum as that observed throughout the sheath region.

2.2. Pressure Exerted by Energetic Protons During the SEP Event

Another feature of this event at PSP was the relatively low magnetic field magnitude observed in the sheath region of ICME-2 as compared with the field intensity measured immediately after the passage of the shock S2 and throughout the passage of ICME-2 (Figure 1(f)). Elevated particle intensities, with a well-ordered energy spectrum, were observed throughout this sheath region (Figure 2). Previous studies have shown that enhanced pressures associated with suprathermal ions can create *craterlike* diamagnetic cavities of depressed magnetic field strengths in the Earth's foreshock region (e.g., Sibeck et al. 2001, 2002). In addition, depressed magnetic field regions where the pressure exerted by energetic particles exceeds both the magnetic field pressure P_B and thermal solar wind pressure P_{TH} are occasionally observed upstream of IP shocks during intense ESP events (e.g., Lario & Decker 2002; Russell et al. 2013; Lario et al. 2015a). So it is reasonable to ask whether the low magnetic fields in the sheath of ICME-2 may be associated with high energetic particle pressure in the sheath.

Figure 3(c) shows the evolution of P_B (red symbols), P_{TH} (blue symbols), and P_{EP} (beige, black, purple, and green traces)

during the SEP event. The magnetic field pressure has been computed as $P_B = B^2/2\mu_0$ (where B is the magnetic field intensity shown in Figure 1(f) and μ_0 is the magnetic permeability). The solar wind thermal pressure is usually computed as $P_{TH} = N_p\,\kappa\,T_p + N_e\,\kappa\,T_e$, where κ is the Boltzmann constant, N_p and T_p are the solar wind proton density and temperature, and N_e and T_e the solar wind electron density and temperature. Owing to the limited plasma data during this period, in addition to neglecting the contribution of heavy ions, we assume charge neutrality $N_p = N_e$ and $T_e = 2T_p$ based on statistical surveys of proton and electron temperatures in post-shock plasmas (e.g., Gosling et al. 1987; Wilson & Chen 2019a, 2019b, 2020).

The pressure P_{EP} exerted by energetic particles has been computed as $P_{EP} = (4\pi/3)(2m)^{1/2}\int_{E_1}^{E_2} E^{1/2}j(E)\,dE$, where E is the proton kinetic energy, $j(E)$ is the proton differential flux, m is the proton mass, and E_1 and E_2 are the limits of the energy range over which P_{EP} is computed. Strictly speaking, the expression used to estimate P_{EP} assumes isotropic particle distributions and should be evaluated in the plasma frame (e.g., Roelof et al. 2010). Energetic particle anisotropies observed downstream of shocks are usually small (e.g., Sanderson et al. 1985, 2000). In fact, for this specific event, isotropic pitch-angle distributions were observed downstream of S2 (see Figure 3 in Giacalone et al. 2021). The limited energy interval available from the particle observations leads us to use $E_1 = 94$ keV as a lower limit to evaluate P_{EP}. Therefore, P_{EP} evaluated between $E_1 = 94$ keV and the highest energy over which the SEP event was observed should be considered as a partial value of the actual pressure exerted by the energetic particles. The expression of P_{EP} computed in the spacecraft frame approximates the correct partial pressure of energetic particles to the order of $\mathcal{O}(U/v)$ where U is the plasma flow speed and v the particle speed (Roelof et al. 2010). Considering that 94 keV protons have a speed of ~ 4200 km s^{-1} and the solar wind speed measured during this event (Figure 1(c)) we estimate $U/v \lesssim 0.1$ upstream of S2, whereas downstream of S2 the uncertainty in P_{EP} can be about ~ 0.2.

In order to evaluate $j(E)$, we have used hourly averages of the ChanR and HET proton intensities displayed in Figure 3(a) covering an energy interval from $E_1 = 94$ keV to $E_2 = 58$ MeV, and assume that $j(E)$ follows the functional form $\propto E^{-\xi}\exp(-E/E_0)$ proposed by Ellison & Ramaty (1985). Figure 3(b) shows the energy spectra at the times A–F indicated in Figure 3(a). Since this functional form seems to underestimate the intensities observed at mid (~ 2–7 MeV) energies, we have assumed also three power laws over the energy ranges 94–221 keV, 0.22–7.67 MeV, and 11.3–58 MeV covered by ChanR and HET. By using the geometric mean energies of each channel to fit the energy spectra and the intersection points between these power laws, we piece together the complete spectrum over the energy interval E_1–E_2. Figure 3(c) shows P_{EP} computed assuming the functional form $\propto E^{-\xi}\exp(-E/E_0)$ (beige traces), and the three power laws (black traces). In order to check the contributions that protons of different energies made to P_{EP}, we also estimate the particle pressure over the energy interval $E_1 = 94$ keV and $E_2 = 5.7$ MeV using the two low-energy power laws and using 5 minute averages of the ChanR intensities (purple trace in Figure 3(c)). Under the assumption that the lowest energy power law can be extended down to 20 keV, we also evaluate P_{EP} over the energy range 20 keV–5.7 MeV (green trace in Figure 3(c)). The lower limit of 20 keV is selected based on the
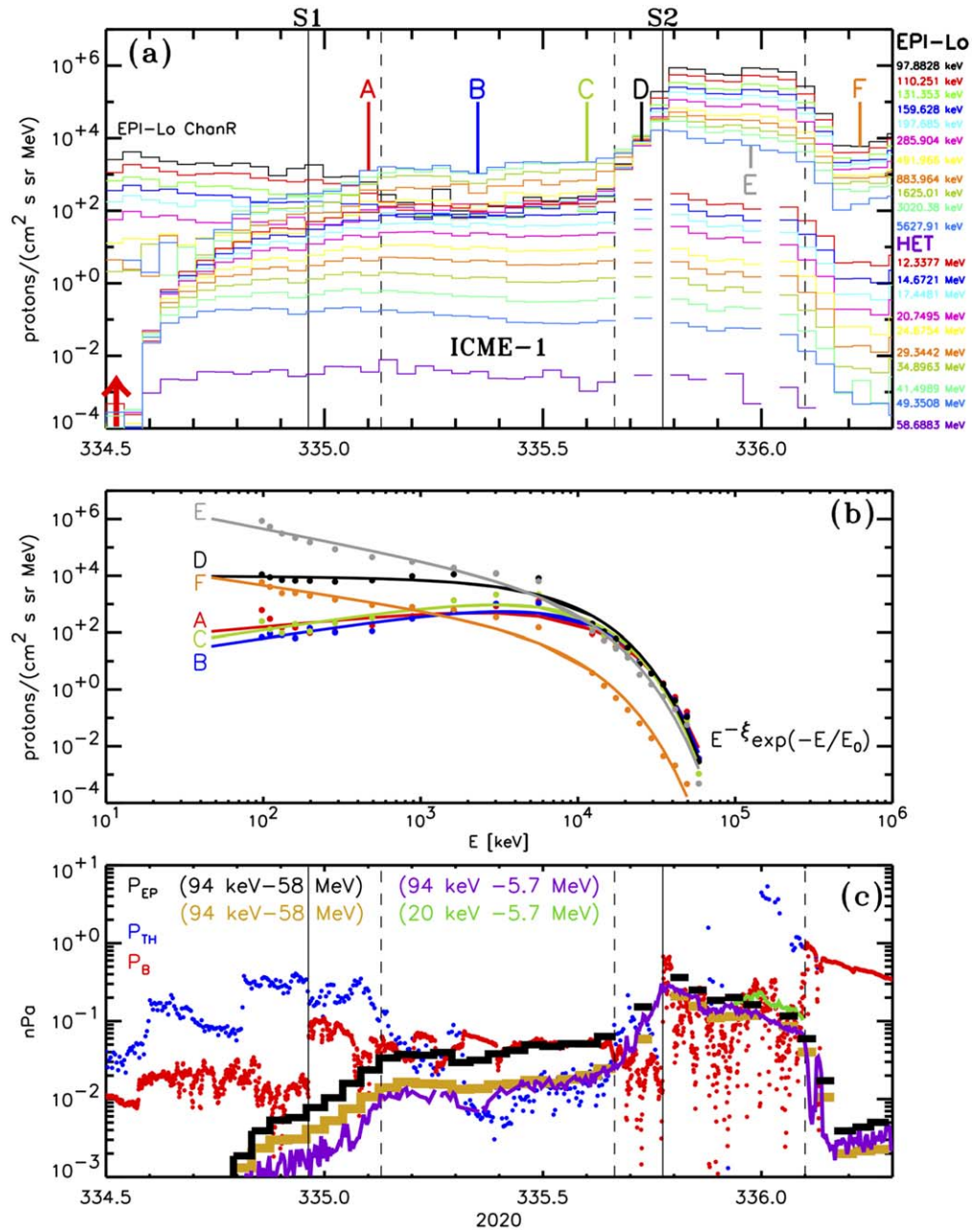
Figure 3. From top to bottom: (a) hourly averages of the proton intensities observed at the different energy channels of the triple coincidence system (ChanR) of EPI-Lo and of the average of the proton intensities measured by EPI-Hi/HET-A and EPI-Hi/HET-B (the listed energies correspond to the geometric mean energy of each channel); (b) energy spectra at the times A–F indicated in the top panel; (c) magnetic field pressure P_B (red symbols); thermal plasma pressure P_{TH} (blue symbols); and partial energetic particle pressure P_{EP} computed assuming for the particle energy spectrum either a functional form $E^{-\xi} \exp(E/E_0)$ (beige trace), three piecewise power laws over the energy interval 94 keV–58 MeV (black trace) and two power laws over the energy interval $E_1 = 94$ keV and $E_2 = 5.7$ MeV (purple trace) and extending the lowest energy power law to 20 keV (green trace).

distinction between thermal and suprathermal populations downstream of fast strong IP shocks (see Figure 8(g) and 10(g) in Lario et al. 2019). The only significant difference between P_{EP} evaluated using this low energy extrapolation and P_{EP} evaluated using the piecewise power-law approximation up to 94 keV is observed in the second half of the sheath region, where P_{EP} increases by a factor $\lesssim 2$. The underestimation of the 2–7 MeV proton intensities by the Ellison–Ramaty functional form may be due to the fact that either the calibration of the intensities in these energy channels is not yet optimal (still being analyzed by the EPI-Lo science team) or that this functional form does not provide an accurate representation of the actual measured energy spectrum. The

former will yield an overestimation of P_{EP} when the observed energy spectrum is approximated by a piecewise power law, whereas the latter does not have a significant effect in the P_{EP} evaluation using the Ellison–Ramaty functional form because of the equal weight given to all energy points when fitting the energy spectra.

With this caveat, Figure 3(c) shows that during the onset of the SEP event and throughout ICME-1, the main contribution to P_{EP} was exerted by $\gtrsim 6$ MeV protons. Throughout this period, P_{EP} remained below P_B. The low temperatures typically observed throughout the passage of an ICME leads to periods with $P_{EP} > P_{TH}$. At the exit of ICME-1, the contribution of

low-energy protons starts to dominate P_{EP}, and throughout the exponential increase of low-energy proton intensities prior to S2, $P_{EP} > P_B$, whereas $P_{EP} \sim P_B$ in the sheath region. The discrete plasma values recovered around the S2 passage suggest $P_{EP} \sim P_{TH}$ when particle fluxes start to increase at the exit of ICME-1, but $P_{EP} < P_{TH}$ in the sheath region. Therefore, the energetic particle pressure in the sheath does not appear to dominate since $P_{EP} \sim P_B$ but $P_{EP} < P_{TH}$. In order to examine whether P_{EP} played an essential role in producing the weak magnetic field observed in the sheath region, we compare this event with other events showing similar magnetic field intensity profiles downstream of IP shocks in Section 4.

3. Events with Preceding ICMEs

As discussed in the previous section, a peculiarity of the 2020 November 29 SEP event at PSP is the in situ observation of an ICME (ICME-1), associated with an earlier CME, during the rising phase of the SEP event that clearly affected the transport of low-energy protons to the spacecraft and hence the observed energy spectra (see Figures 1 and 2). In this section, we analyze similar SEP events observed at 1 au where an intervening ICME was observed preceding the arrival of an IP shock with elevated particle intensities.

A well-known case is the Bastille Day event on 2000 July 14 that has been widely studied by several authors (e.g., Smith et al. 2001; Lepping et al. 2001). Figure 4 shows, with the same format as Figure 1, particle, plasma, and magnetic field data collected by near-Earth spacecraft during this event. In particular we show (a) ion data collected by the Low-Energy Magnetic Spectrometer (LEMS120) of the Electron Proton Alpha Monitor (EPAM) on board the Advanced Composition Explorer (ACE/EPAM/LEMS120; Gold et al. 1998) and the energetic particle sensor (EPS) on board the Geostationary Operational Environmental Satellite GOES-8 (Sauer 1993); (b) 103–175 keV electron intensities measured by the deflected electron detector (DE) of ACE/EPAM (Gold et al. 1998) and 0.7–3.0 MeV electron intensities measured by the Electron, Proton Helium Instrument (EPHIN) of the Comprehensive Suprathermal and Energetic Particle Analyzer (COSTEP) on board SOHO (SOHO/COSTEP/EPHIN; Müller-Mellin et al. 1995); solar wind proton (c) speed, (d) density, and (e) temperature measured by the Solar Wind Electron, Proton, and Alpha Monitor (SWEPAM) on board ACE (ACE/SWEPAM; McComas et al. 1998); and magnetic field (f) magnitude and (g–h) angular direction in the spacecraft-centered RTN coordinated system measured by the magnetometer experiment on board ACE (ACE/MAG; Smith et al. 1998). During periods of large SEP intensities, data from ACE/SWEPAM exist only in its *search* mode that collects data at approximately every ~33 minutes (Skoug et al. 2004). These data are plotted as thick blue symbols in Figures 4(c)–(e).

This SEP event was associated with a fast halo CME, with a plane-of-sky speed of 1674 km s^{-1} in the CDAW catalog, first observed by SOHO/LASCO at 10:54 UT on 2000 July 14 (day of year 196) and temporally associated with an X5.7 flare at 10:21 UT on the same day from AR 9077 at N22W07 (Andrews 2001). The leading edge of the associated ICME arrived at ACE at ~19:00 UT on day 197 (implying an average transit speed of ~1268 km s^{-1}) and was preceded by a shock that passed ACE at 14:16 UT on day 197 (average transit speed of ~1482 km s^{-1}). We have labeled the passages of this shock and ICME at ACE in Figure 4 as S2 and ICME-2, respectively.

Shock S2 was preceded by an ICME (ICME-1 in Figure 4) with leading edge at ~17:00 UT on day 196 and upstream shock (S1) at 14:59 UT. The trailing edge of ICME-1 is drawn at the passage of S2. We note that Lepping et al. (2001) set the trailing edge of ICME-1 at ~14:00 UT on day 197 just before the arrival of S2 based on a model fitting for the magnetic cloud seen inside ICME-1 using hourly averaged magnetic field data (see their Figure 3). However, other ICME-like characteristics were observed until just before the arrival of S2 (Smith et al. 2001). Thus, a difference between the PSP event and the Bastille Day event is that, in the case of the Bastille Day event, S2 was propagating into the trailing edge of ICME-1, whereas for the 2020 November 29 event at PSP, S2, and ICME-1 were separated by ~2.65 hr based on the magnetic field and limited plasma observations available used to identify ICME-1 (Figure 1).

As for the SEP event at PSP, the onset of the Bastille Day SEP event occurred shortly before the passage of shock S1, where there is a slight distortion of the particle intensity-time profiles. Within ICME-1, the intensities of $\lesssim 30$ MeV protons and $\lesssim 300$ keV electrons kept increasing until the arrival of S2, whereas the higher-energy proton and electron intensities remained flat or slightly decreased throughout ICME-1. The rising intensity profiles observed throughout ICME-1 suggest that particles accelerated by S2 were able to gain entry into ICME-1 from early in the event, even when S2 was still close to the Sun. The access of particles accelerated by S2 into ICME-1 may have occurred by processes of cross-field diffusion or by a portion of the shock S2 propagating into ICME-1.

A significant difference between the Bastille Day event and the PSP event is the low-energy particle signatures observed at the entry into and exit from ICME-1. Whereas in the PSP event, the entry into and exit from ICME-1 were associated with interruptions in the evolution of the low-energy particle intensities and energy spectra (Figure 2), the Bastille Day event did not show such discontinuities. Two factors may play a role in these observed differences: First, PSP observations shown in Figure 2 were derived from the triple coincidence system of EPI-Lo that cleanly excludes higher-energy particle counts, whereas the ACE/EPAM/LEMS120 intensities shown in Figure 4 include contributions from electrons and high-energy particles (Marhavilas et al. 2015) that form an intensity background that precludes the observation of complete particle intensity depressions. Second, the difference at the exit of ICME-1 between the Bastille Day event and the PSP event may be due to the fact that, at its arrival at ACE, the shock S2 for the Bastille Day event was already within ICME-1 and able to fill ICME-1 with shock-accelerated particles, whereas at PSP the separation between ICME-1 and S2 did not allow the low-energy particles to penetrate into ICME-1. We should also note that since ICMEs and IP shocks are large-scale structures, the single-point observations from either ACE (Figure 4) or PSP (Figure 1) may not reflect the configuration of ICME-1 and S2 as a whole.

With the purpose of finding additional cases of IP shocks with elevated particle intensities preceded by the passage of an ICME, we have combined the list of ICMEs in the Near-Earth ICME catalog posted on www.srl.caltech.edu/ACE/ASC/ DATA/level3/icmetable2.html (Richardson & Cane 2010a) with observations of SEP events with intense ESP components. SEP events associated with the passage of IP shocks with
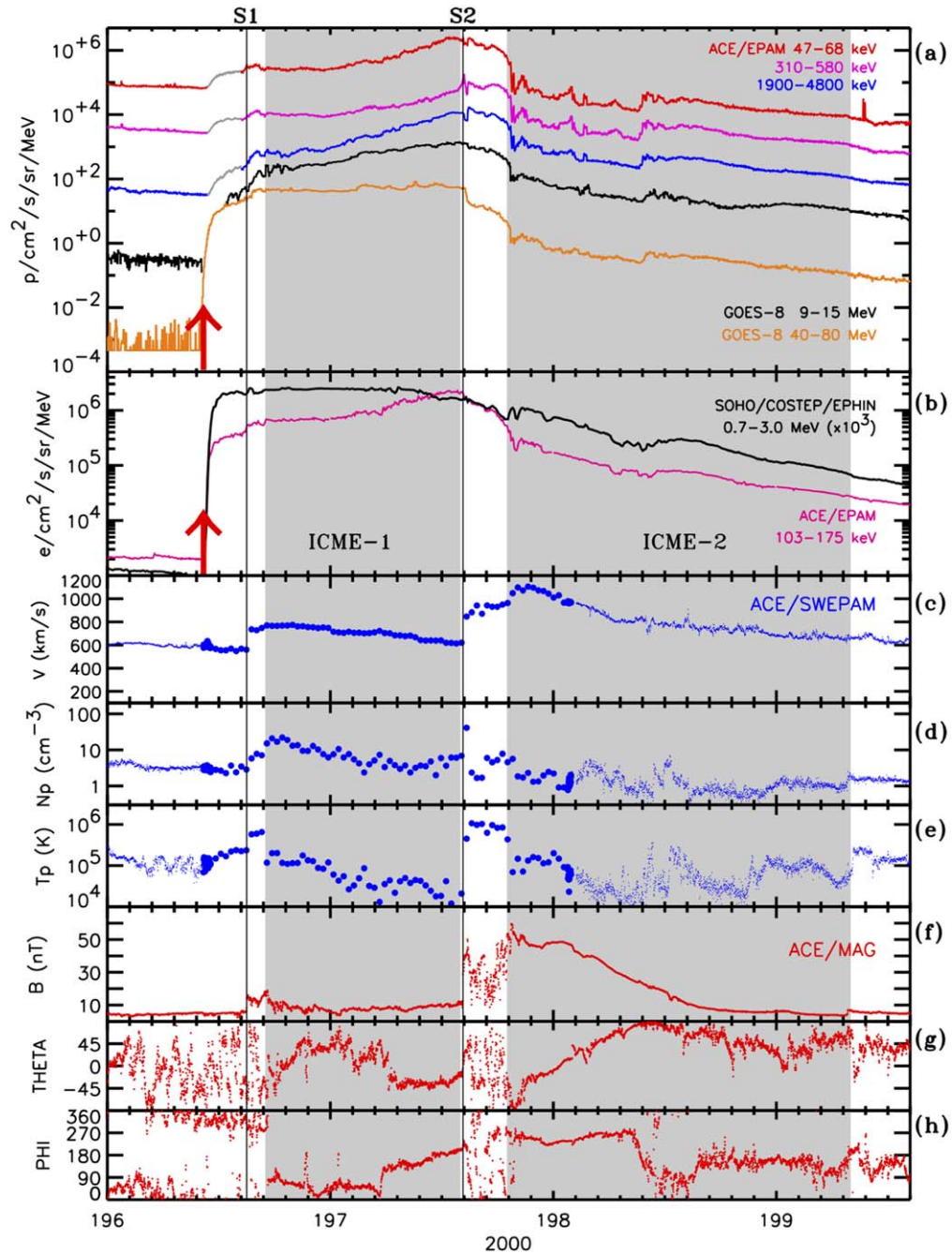
Figure 4. From top to bottom: (a) 5 minute averages of the omni-directional proton intensities observed by ACE/EPAM/LEMS120 (three top traces) and EPS of GOES-8 (two bottom traces); (b) 5 minute averages of the electron intensities observed by ACE/EPAM/DE and 30 minute averages of the electron intensities (multiplied by a factor 10^3) measured by SOHO/COSTEP/EPHIN; proton solar wind (c) speed, (d) density, and (e) temperature obtained from ACE/SWEPAM measurements; and magnetic field (f) magnitude, (g) elevation angle, and (h) azimuth angle in RTN coordinates as measured by ACE/MAG. The solid vertical lines identify the passages of shocks and the shaded gray bands the passages of ICMEs. The red arrows in (a) and (b) indicate the onset of the X5.7 solar flare temporally associated with the origin of the SEP event. The large solid blue symbols in panels (c)–(e) were obtained from the search mode of ACE/SWEPAM. The gray portions of the ACE/EPAM/LEMS120 ion traces in panel (a) indicate periods with possible electron contamination.

intense ESP components are usually associated with fast CMEs generated from longitudes close to central meridian (Smart & Shea 1996; Mäkelä et al. 2011). CMEs are then likely to interact with or overtake any preceding slower ICMEs that are present. Therefore, cases similar to that observed by PSP at ~0.8 au, with some delay between the passage of the trailing edge of the preceding ICME-1 and the shock S2, are rare, especially at larger heliocentric distances when the probability of ICME–ICME interaction increases (Lugaz et al. 2017).

However, Figure 5 shows two such events observed at ~1 au (following the same format as Figure 4) where an IP shock associated with an intense ESP event was preceded by an ICME (ICME-1) with the trailing edge arriving just a few hours before the shock.

The SEP event on the left column of Figure 5 was generated by a fast CME (CDAW plane-of-sky speed 1333 km s^{-1}) temporally associated with an M2.2 flare with onset at 13:37 UT on 2004 July 25 (day of year 207) from AR 10652
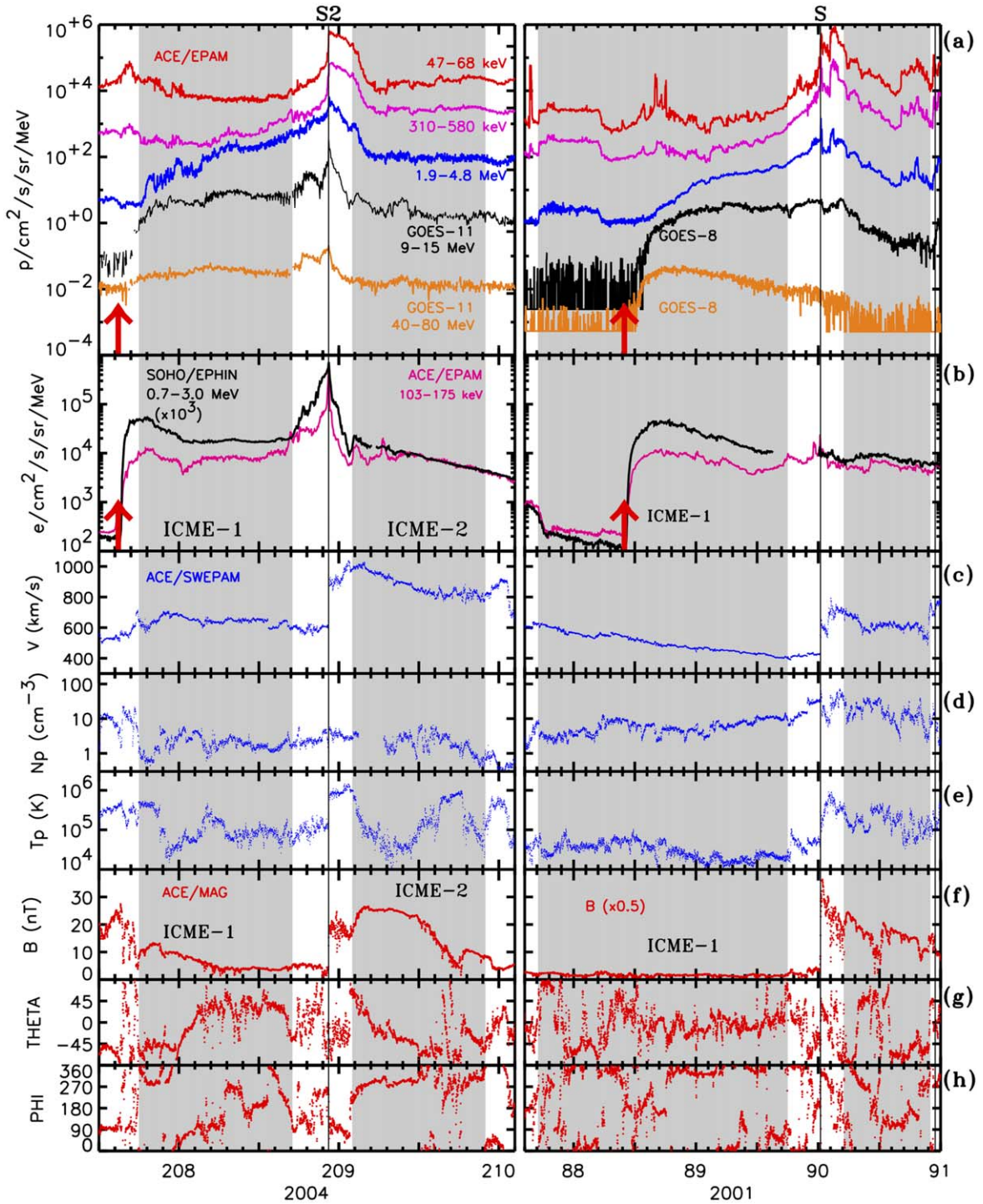
Figure 5. The same as Figure 4 for the SEP events on (left) day 207 of 2004 and (right) day 88 of 2001.

at N04W30 (red arrow in the left panels of Figure 5(a) and (b)). ICME signatures such as the magnetic field rotation and solar wind proton temperature depression observed late on day 207 and throughout most of day 208 were used to identify the passage of the ICME-1 that preceded the passage of an IP shock (S2) by ACE at 22:27 UT on 2004 July 26 (day of year 208). The existence of a gap of ∼5.4 hr between the trailing edge of ICME-1 and shock S2 was also established by examining solar wind ion charge state observations from ACE/SWICS (not shown here), which show a change from the high charge states associated with the ICME to more normal solar

wind charge states consistent with the ICME-1 trailing edge indicated in the left column of Figure 5.

Some features of the SEP event on day 207 of 2004 resemble those of the PSP event. Low-energy ≲200 keV ion intensities were reduced throughout the passage of ICME-1 as shown by the 47–68 keV ion intensity-time profile (red trace in Figure 5(a)). Low-energy ion counts within ICME-1 do not go to discrete singular counts as in the PSP case because, in contrast to the triple coincidence system that excludes higher-energy particle counts, ACE/EPAM/LEMS120 intensities have a background owing to high-energy particle contributions.

Particle depressions during ICME passages are more easily noticeable when there is an enhanced low-energy ion population outside of the ICME emphasizing the contrast between internal and external intensities. Similarly to the PSP event, the $\lesssim 200$ keV proton intensities in the event on day 207 of 2004 increased at the exit from ICME-1. The event on day 207 of 2004 differs from the PSP event in that, throughout the passage of ICME-1, the $\gtrsim 300$ keV proton intensities increased continuously up to the arrival of S2, and that the $\gtrsim 9$ MeV ion intensities showed abrupt increases in the rate of change with time at the trailing edge of ICME-1, leading up to a clear intensity peak at shock S2, which is also evident for >40 MeV protons and ~ 1 MeV electrons. The gaps and time resolution of the EPI-Hi/HET data preclude us from determining whether a localized high-energy particle peak was also present near S2 at PSP (see Figure 1).

Another case with a delay between the passage of an IP shock and a preceding ICME was observed in March 2001, though the situation in this event also differs from that of the 2020 November 29 event at PSP. The SEP event shown in the right column of Figure 5 was generated by a fast CME (CDAW plane-of-sky speed 942 km s^{-1}) temporally associated with a X1.7 flare at 09:57 UT on 2001 March 29 (day of year 88) from AR 9393 at N14W12. In contrast to the PSP event and other events considered here, the onset of the SEP event occurred during the passage of an ICME (ICME-1 in the right column of Figure 5). A delay of ~ 6.3 hr was observed between the trailing edge of ICME-1 and the passage of the shock at 00:23 UT on day 90 (identified by S in Figure 5). The exit from ICME-1 is marked only by small increases in the slopes of the $\lesssim 10$ MeV proton and $\lesssim 300$ keV electron intensity-time profiles that keep increasing until the arrival of the shock (unfortunately a data gap in the SOHO/COSTEP/EPHIN data does not allow us to determine the evolution of the high-energy electron intensity between ICME-1 and the arrival of the shock). Therefore, the evolution of the particle intensities across the trailing edge of this preceding ICME is more continuous than that observed in the PSP event.

The events in Figure 5 suggest that there is no consistent behavior in the particle intensities at the trailing edge of the preceding ICME (ICME-1). In one case, the trailing edge is apparently transparent, and no intensity change is observed, whereas in the other case, a clear discontinuity is present, in particular for low-energy ions and near-relativistic electrons. The events in Figure 5 also highlight the need for measurements that are clean of high-energy particle contributions (such as those shown in Figure 2) in order to reveal whether low-energy particles are excluded from ICMEs.

4. Particle Pressure Effect on Sheath Properties

The other interesting feature of the event at PSP is the low magnetic field magnitude observed in the sheath of ICME-2 (see Figure 1(f)). The partial pressure exerted by energetic particles P_{EP} measured at PSP showed values similar to P_B throughout the sheath region, whereas the sparse plasma data seem to indicate that $P_{EP} < P_{TH}$ (see Figure 3(c)). In order to determine whether energetic particles might have played a dominant role in the depletion of magnetic field strength in the sheath region, we analyze here several intense ESP events with similar magnetic field profiles in the sheath regions and for which more complete plasma observations are available that may provide an analog for the PSP event.
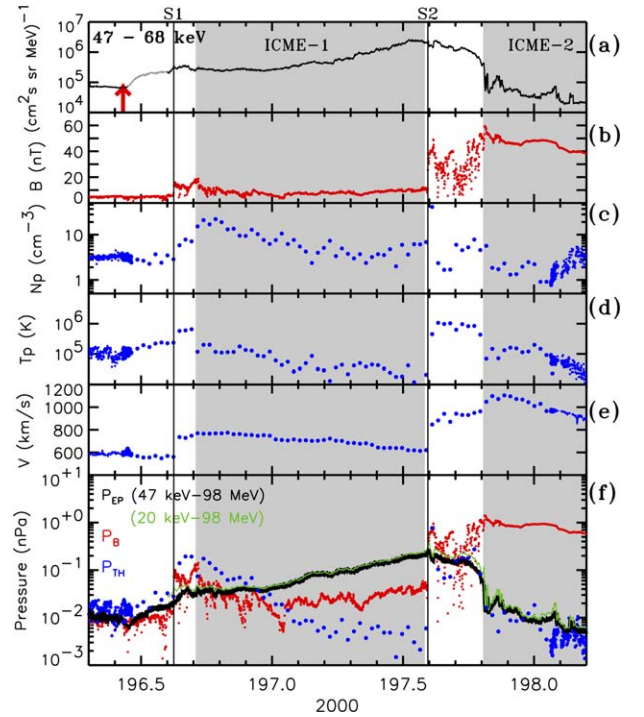

Figure 6. ACE observations during the Bastille Day 2000 event. (a) 1 minute averages of 47–68 keV ion spin-averaged intensities measured by ACE/EPAM/LEMS120; (b) 64 s averages of the magnetic field magnitude observed by ACE/MAG; (c) solar wind proton density, (d) temperature, and (e) speed measured by ACE/SWEPAM in its normal mode (64 s averages) or in its search mode (discrete blue symbols); (f) magnetic field pressure P_B (red), solar wind thermal pressure P_{TH} (blue), and energetic particle partial pressure P_{EP} computed combining ACE/EPAM/LEMS120 and GOES-8/EPS data over the energy interval 47 keV–98 MeV (black) or extrapolating the energy spectrum down to 20 keV (green). The solid vertical lines indicate the passage of IP shocks labeled S1 and S2 and the shadowed gray bars the passage of ICMEs.

Similarly to the PSP event, magnetic fields in the sheath region of ICME-2 in the Bastille Day event were weak compared to those measured just behind the shock S2 and within ICME-2 (Figure 4(f)). Figure 6 shows, from top to bottom, (a) spin-averaged 47–68 keV ion intensities measured by ACE/EPAM/LEMS120, (b) magnetic field magnitude B, (c) solar wind proton density N_p, (d) temperature T_p, and (e) speed V as measured by ACE during the Bastille Day event. Figure 6(f) shows the magnetic field pressure P_B (red symbols), the thermal pressure P_{TH} (blue symbols), and the partial pressure exerted by energetic particles P_{EP} (black and green traces). In order to compute P_{EP}, we have combined ACE/EPAM/LEMS120 and GOES data and followed the same procedure as described in the explanation of Figure 3 using the expression $E^{-\xi} \exp(-E/E_0)$ over the energy interval 47 keV–98 MeV (black trace). We have also extrapolated these energy spectra down to 20 keV to extend the lower energy limit in our estimation of P_{EP} (green trace). Similarly to the PSP event (see Figure 3(c)), the only significant difference in P_{EP} using the two different energy intervals is observed in the second half of the sheath region. During the sheath region of the Bastille Day event, we see that $P_{EP} \sim P_{TH}$ but $P_B \gtrsim P_{EP}$. By contrast, upstream of S2 and during the second half of ICME-1, P_{EP} was well above P_{TH} and P_B. This suggests that the effects of energetic particles on the magnetic field properties in the sheath during the Bastille Day event did not play a dominant role.
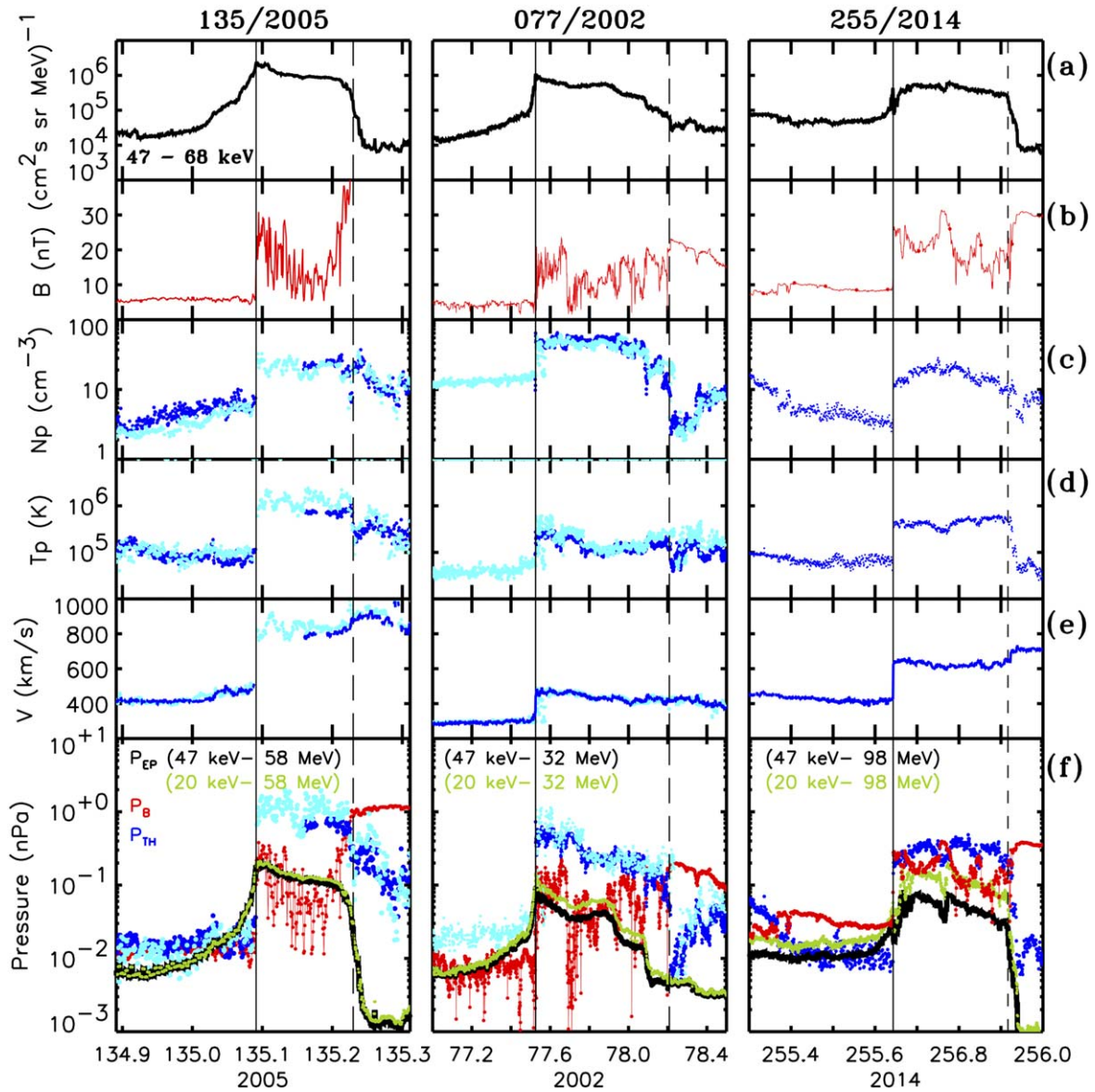
Figure 7. The same format as Figure 6 but for the ESP events on, from left to right, day 135 of 2005, 77 of 2002, and 255 of 2014. Dark blue symbols in panels (c) through (f) use measurements from ACE/SWEPAM, whereas cyan symbols use measurements from Wind/SWE shifted to the time of the shock passage (solid vertical line) at ACE. The dashed vertical lines indicate the leading edge of the ICMEs.

Figure 7 shows three other examples of intense ESP events (using the same format as Figure 6, except that the plasma parameters in (c)–(f) are from both ACE/SWEPAM (dark blue symbols) and from the Solar Wind Experiment (SWE; Ogilvie et al. 1995) on board the Wind spacecraft (cyan symbols) shifted to the time of the shock passage at ACE). In these three cases, the magnetic field in the sheath downstream of the IP shock (indicated by the vertical solid lines) and prior to the arrival of the following ICME (indicated by the vertical dashed lines) shows periods with depressed magnitude. In each case, the low-energy ion intensity is elevated in the sheath and falls abruptly on entry to the ICME, as in the PSP event. In these events, $P_{EP} < P_{TH}$ throughout the sheath regions. During the event on day 135 of 2005 (left column in Figure 7) P_{EP} exceeded P_B only in the portion of the sheath with depressed magnetic field. In the sheath region of the event on day 77 of 2002 (middle column in Figure 7), P_{EP} remained mostly below P_B. Finally in the event on day 255 of 2014 (right column in

Figure 7), B was most strongly depressed in the trailing half of the sheath but P_{EP} reached values similar to P_B only when the spectrum extrapolation to low energies is considered. In these three events with relatively weak magnetic fields but enhanced energetic particle intensities in the sheath similar to the PSP event, we see that P_{EP} in the sheath region remained well below P_{TH}, and that variations of the energetic particle pressure did not correlate with variations of the magnetic field magnitude. On the other hand, with the exception of the events on day 255 of 2014 (right column in Figure 7) and on day 090 of 2001 (right column in Figure 5), all the intense SEP events shown here had $P_{EP} > P_B$ immediately upstream of the shock. A similar pattern in which the energetic particle pressure in an intense SEP event dominates over the magnetic field pressure just before arrival of a shock but not downstream of the shock has been observed in past studies (e.g., Lario et al. 2015a, 2015b, and references therein).

5. Discussion

Two of the distinctive features of the 2020 November 29 SEP event at PSP were the inverted energy spectra observed during the passage of ICME-1 (see Figure 2) and the low magnetic field magnitude observed in the sheath of ICME-2 where high particle intensities were present (see Figure 1). Here we discuss, in the light of observations of previous SEP events observed near Earth, possible reasons for these two peculiarities and the role that ICME-1 played in these singular observations.

5.1. Exclusion of Low-energy Ions from ICME-1

The discontinuity in the energetic particle spectra coincident with the passage of the ICME-1 at PSP (Figure 2) as well as the depression of low-energy ($\lesssim 220$ keV) proton intensities suggest that the low-energy ions were effectively excluded from ICME-1. One of the energetic particle signatures associated with the passage of ICMEs (e.g., Richardson 1997) is a depression in the energetic particle intensities observed upon the entry of the spacecraft into the ICME with respect to those measured prior to the passage of the ICME. The relative sizes of the energetic particle depressions in ICMEs, which can occur from galactic cosmic ray energies in Forbush decreases to tens of keVs, display a rigidity dependence (Cane et al. 1995; Belov et al. 2021). The small Larmor radius of low-energy protons (for example, a 220 keV proton with a 90° pitch-angle in a 10 nT magnetic field has a Larmor radius of only ~4.5×10^{-5} au) forces these particles to sample the fine structure of the IP disturbances as they propagate through IP space, and precludes them from penetrating into an ICME via their gyromotion from remote distances. By contrast, the larger the Larmor radius and the speed of the particles, the more efficiently the particles can penetrate across the boundaries of the ICMEs into the closed structures assumed for ICMEs (e.g., Laitinen & Dalla 2021).

The fact that ICME-1 and ICME-2 started propagating from different regions (ICME-1 from AR 12787 at N32E89 and ICME-2 from AR 12790 at S23E99), and that, at the time of the M4.4 flare, the leading edge of ICME-1 was already at ~0.7 au from the Sun (assuming that it propagated at a speed of 572 km s^{-1} as inferred from coronagraph observations), implies that the shock S2 did not establish direct magnetic connection with the interior of ICME-1 when it formed close to the Sun. However, the fact that the intensity-time profiles of high-energy ($\gtrsim 20$ MeV) protons did not show clear discontinuities across the leading edge of ICME-1 (see Figure 3(a)) and that the intensities of protons with energies between 220 keV and ~15 MeV increased close to the entry of the spacecraft into ICME-1 (Figures 2 and 3(a)) suggests that, at some point during its propagation, particles accelerated by the shock S2 penetrated into ICME-1. The peculiarity is that $\lesssim 200$ keV protons were excluded from ICME-1, showing a clear intensity depression (increase) at the passage of the leading (trailing) edge of ICME-1 (see Figure 2(a)).

The study of particle intensity variations across the edges of ICMEs requires a precise identification of the ICME boundaries. This identification is usually based on the discontinuous evolution of different signatures commonly used to determine the passage of ICMEs (e.g., Zurbuchen & Richardson 2006). Whereas the front boundary of ICMEs usually shows clear discontinuities in these signatures, the rear boundaries are more difficult to identify and sometimes their determination is rather subjective and depends on the specific ICME signatures considered (Neugebauer & Goldstein 1997). In this particular case, the leading edge of ICME-1 was identified with a discontinuity of the magnetic field orientation that coincided with a relative decrease of solar wind density and temperature. The trailing edge of ICME-1 was identified with an increase of T_p and change in the magnetic field direction that coincided with (1) a small depression of the magnetic field strength, (2) a low-energy proton intensity exponential increase upstream of S2, and (3) a discontinuity in the evolution of the energy spectrum.

Exponentially rising low-energy particle intensity enhancements upstream of IP shocks followed by approximately constant intensity downstream, as observed by PSP for the shock S2, are qualitatively consistent with DSA predictions, where waves amplified by the shock-accelerated particles contribute to confine the shock-accelerated particles in the foreshock region (e.g., Lee 2005). Whereas an exponential particle increase is usually observed at strong IP shocks (e.g., Giacalone 2012), the onset of this increase is not usually accompanied by large-scale discontinuities in the magnetic field (see, e.g., Figures 2, 3, and 4 in Giacalone 2012). An exception occurs in especially intense ESP events (see Figures 1 and 4 in Lario et al. 2015a) where magnetic field depletions may be observed immediately before the shock, exactly at the time when low-energy particle intensities show a pronounced increase before the arrival of the shock. It is at these times when $P_{EP} > P_B$ might be observed (Lario et al. 2015a), suggesting that energetic particles may also contribute to intensify the observed upstream field depressions (Sibeck et al. 2001). PSP observations upstream of the shock S2 are consistent with such a scenario.

The access of high-energy protons into ICME-1 from early in the event (Figure 1(a)) may result from either a portion of the shock S2 being able to interact with ICME-1 and accelerate particles within this structure or from cross-field diffusion and drift transport processes undergone by the particles near the boundaries of ICME-1. In either case, the observed intensity-time profiles at PSP are a consequence of the evolving efficiency of shock acceleration for particles of different energies, the magnetic connection established between the spacecraft and the shock, and the processes that transported SEPs before they reached the spacecraft. The possibility that the shock S2 at PSP propagated within ICME-1 would imply that low-energy ($\lesssim 220$ keV) protons remained confined just upstream of the shock S2, whereas higher-energy protons propagated throughout ICME-1. Such a confinement of low-energy protons near the shock may be caused by either waves amplified by the shock-accelerated particles or by an intervening structure formed just in front of the shock S2. The amplification of waves by shock-accelerated particles requires a preexisting level of turbulence (Lee 2006), but the smooth magnetic field usually observed within ICMEs (allowing the scatter-free transport of energetic particles; e.g., Torsti et al. 2004) is not consistent with the presence of this preexistent turbulence level. The presence of an intervening structure within ICME-1 with depressed magnetic field intensified by the effect of energetic particles cannot be discarded. However, the discontinuities in the field magnitude and orientation as well as in the solar wind temperature used to identify the trailing edge of ICME-1 in Figure 1 are signatures usually adopted to

distinguish ICMEs structures from the regular solar wind. Therefore, we argue that at its arrival at PSP the portion of the shock S2 observed by PSP did not intercept ICME-1 and that there was an actual delay between the passage of the trailing edge of ICME-1 and the shock S2.

In contrast, the shock S2 in the Bastille Day event was observed, when it arrived at 1 au, to be at or within the trailing edge of ICME-1. This is consistent with the fact that energetic particle intensities increased throughout ICME-1 peaking with the arrival of the shock S2. Although P_{EP} exceeded P_B in a large portion of ICME-1 (see Figure 6(f)), no abrupt discontinuity was observed in the particle intensities or energy spectra within ICME-1. Therefore, we believe that the distinction between the Bastille Day event and the PSP event was whether S2 interacted with ICME-1, being able to fill with energetic particles ICME-1 in the Bastille Day event where even the lowest energy ions propagated within ICME-1, but not in the PSP case.

Whereas the shock S2 in the Bastille Day event was observed at the trailing edge of a preceding ICME, the presence of IP shocks propagating within ICMEs is not an uncommon phenomenon (e.g., Lugaz et al. 2015). However, the observations of particle intensity enhancements associated with these intra-ICME shocks are infrequent. For example, Xu et al. (2019) searched for proton intensity enhancement between ∼200 keV and ∼7 MeV using Wind/3DP (Lin et al. 1995) data inside 487 ICMEs between 1995 and 2017, and found only a total of 12 ICMEs with energetic particle enhancements with respect to the proton intensity measured upstream and downstream of the ICME, nine of which included shocks propagating into the ICMEs. Other notable cases are those reported by Shen et al. (2008), Richardson & Cane (2010b), and Bruno et al. (2019). Cases where an intra-ICME particle enhancement was due to a new SEP event (such as the event in the right column of Figure 5) were excluded in these statistics.

Usually the particle intensity enhancements produced by shocks propagating inside an ICME fill the whole ICME, with low-energy particle intensities increasing on entry of the spacecraft into the ICME (see Figures 3 and 4 in Li & Lugaz 2020). An analytical model of time-dependent DSA inside magnetic clouds has been developed by Li & Lugaz (2020). This suggests that, in order to generate large particle enhancements, the shock has to propagate within the ICME for an extended time period before its arrival at the observer. Particle acceleration by a shock inside an ICME is also favored if there is a preexisting seed particle population present in the ICME. These particles may result from previous SEPs that were directly injected into the ICME as it propagated through IP space (such as the event in the right column of Figure 5; see also Richardson & Cane 1996) or from the cross-field diffusion of particles into the ICME (such as in the events of Figures 1, 4, and the left column of Figure 5).

This study also illustrates that the trailing edges of ICMEs may have different effects on the particle populations. At the trailing edges of ICME-2 in the PSP event (Figure 1), the Bastille Day event (Figure 4), and the event on 207 of 2004 (left column in Figure 5) there was no change in the rate at which the particle intensities decayed. In order to see the contrast between internal and external particle populations it is necessary to have a nearby source of particles such as those provided by S2 for the preceding ICME-1. The energy dependence in the process of particle penetration into ICMEs

may depend not only on the properties of the boundaries of the ICMEs and the scattering conditions of the particles around the ICMEs (e.g., Laitinen & Dalla 2021), but also on the proximity and time availability of the shock S2 to fill ICME-1 with particles of different energies before reaching the spacecraft. The variability of intensity-time profiles observed across the edges of the ICMEs (see Figure 5) may result from these varying conditions. However, in order to clearly see an inversion of the energy spectra within an ICME (such as that observed by PSP; Figure 2), measurements free of high-energy particle contributions (such as the triple coincidence measurements provided by EPI-Lo) are required. Existing background produced by high-energy particles in the ACE/EPAM/ LEMS120 measurements does not allow seeing this inverted spectrum but just some intensity depression within ICMEs such as that seen in the 47–68 keV ion intensities in the event on day 207 of 2004 (left column in Figure 5).

5.2. Magnetic Field Properties in the Sheath Region

The sheath region in front of an ICME is typically characterized by dense and disturbed solar wind. Fast ICMEs, exceeding the magnetosonic speed in the solar wind, may drive shock waves that compress the upstream ambient solar wind material, resulting in sheath regions with much more enhanced density and temperature as well as larger magnetic field fluctuations than those observed in sheaths not preceded by shocks (e.g., Salman et al. 2020). It has been suggested that the material found in the sheath region of ICMEs may be composed of coronal or heliospheric compressed material (Howard & Vourlidas 2018). By comparing the geometry of CMEs inferred from coronagraph images with the in situ properties of ICMEs, Temmer et al. (2021) showed that the sheath region does not consist of coronal CME plasma but pile-up material coming from the preceding solar wind plasma. Whereas the magnetic ejecta region depends on the CME properties at the Sun, the sheath structures have a strong dependence on the conditions ahead of the disturbance. The amount of piled-up mass (and hence the density measured in the sheath) depends on the pre-event ambient material (denser when the ICME propagates in slow solar wind than when propagates in fast wind), and on the size of the ICME (wider CMEs may pile up more material, whereas in narrow CMEs the upstream solar wind may more easily flow around). Temmer et al. (2021) argued that the ICME IP propagation speed is not related to the sheath density, and that the size of the ICME may play some role in how much material could be piled up. In fact, statistical studies have found that the magnetic field strength in the sheath is only moderately correlated with the average magnetic field strength and speed of the ICME (Chi et al. 2016; Salman et al. 2020).

Therefore, the signatures and properties of the sheath regions depend strongly on the ambient solar wind properties, as well as how far from the apex of the ICME the spacecraft crosses the sheath region (Janvier et al. 2015). Close to the shock, field fluctuations seem to be associated with the shock compression process and with the alignment of preceding ambient fluctuations, whereas far from the shock field fluctuations are more evolved, and near the leading edge of the ICME the field line wrapping might intensify the field again (e.g., Kilpua et al. 2021, and references therein). Therefore, the oscillating character of the magnetic field in the sheath regions observed in the events seems to be more a consequence of the medium

where the IP shock propagates rather than the effect of the shock-accelerated particles. Indeed, the events shown in Figure 7 showed that P_{EP} does not correlate with the oscillating values of P_B, indicating that variations in B are not driven by changes in the energetic particle pressure. The fact that we can find sheaths with oscillating low magnetic fields but with $P_{EP} < P_B$ suggests that P_{EP} is not the dominant factor determining the field properties within the sheath region. The caveat is that our evaluation of P_{EP} is an estimate of the actual pressure exerted by energetic particles because of the approximations made in its computation.

For the SEP events described in Sections 2 and 3, the shock S2 propagated in the wake of a preceding ICME, that is usually characterized by rarefaction regions and weakened magnetic field (e.g., Liu et al. 2014). Therefore, we argue that the upstream medium found ahead of ICME-2 played a more important role in the properties of the sheath region than the effect of the energetic particles.

6. Summary

The two interesting features of the SEP event observed by PSP from 2020 November 29–December 2 analyzed in this work can be summarized as follows:

1. The shock S2 associated with the CME on 2020 November 29 that generated the SEP event commencing on this day, was preceded when it arrived at PSP by an intervening ICME (ICME-1) that modified the low-energy ion intensity-time profile and energy spectra. PSP observations from EPI-Lo showed that low-energy ($\lesssim 220$ keV) protons accelerated by S2 were excluded from ICME-1, resulting in the observation of inverted energy spectra during the passage of ICME-1. Comparison with other similar events shows that the properties of the ICME-1 trailing edge and the proximity and possible penetration of the shock S2 into the ICME-1 are the main factors that determine the influence of the preceding ICMEs on the transport of shock-accelerated particles toward the spacecraft. The inverted spectra are shown particularly well in the triple coincidence EPI-Lo observations, which are not contaminated by heavy ions or high-energy particles. This event clearly demonstrates that the influence of unrelated solar wind structures should be considered when studying SEP event intensity-time profiles.

2. The sheath region behind the shock S2 was characterized by weak but fluctuating magnetic fields. Whereas upstream of S2 the partial pressure exerted by energetic particles exceeded the magnetic field pressure, behind the shock both pressures were similar. Comparison with events observed by near-Earth spacecraft showing similar sheath magnetic fields reveals that variations in magnetic field pressure are not correlated with variations in the energetic particle pressure, and low magnetic field strengths are observed even when particle pressures are relatively low. Therefore, with the caveat that our estimates of the energetic particle pressure are approximations of the actual pressure exerted by energetic particles, we argue that P_{EP} did not play a dominant role in determining the field properties of the sheath region but instead, the weak sheath magnetic fields reflect conditions in the solar wind plasma upstream of the shock that is propagated into the sheath.

ORCID iDs

D. Lario ⓘ https://orcid.org/0000-0002-3176-8704
I. G. Richardson ⓘ https://orcid.org/0000-0002-3855-3634
E. Palmerio ⓘ https://orcid.org/0000-0001-6590-3479
N. Lugaz ⓘ https://orcid.org/0000-0002-1890-6156
S. D. Bale ⓘ https://orcid.org/0000-0002-1989-3596
M. L. Stevens ⓘ https://orcid.org/0000-0002-7728-0085
C. M. S. Cohen ⓘ https://orcid.org/0000-0002-0978-8127
J. Giacalone ⓘ https://orcid.org/0000-0002-0850-4233
D. G. Mitchell ⓘ https://orcid.org/0000-0003-1960-2119
A. Szabo ⓘ https://orcid.org/0000-0003-3255-9071
T. Nieves-Chinchilla ⓘ https://orcid.org/0000-0003-0565-4890
L. B. Wilson, III ⓘ https://orcid.org/0000-0002-4313-1970
E. R. Christian ⓘ https://orcid.org/0000-0003-2134-3937
M. E. Hill ⓘ https://orcid.org/0000-0002-5674-4936
D. J. McComas ⓘ https://orcid.org/0000-0001-6160-1158
R. L. McNutt, Jr. ⓘ https://orcid.org/0000-0002-4722-9166
N. A. Schwadron ⓘ https://orcid.org/0000-0002-3737-9283
M. E. Wiedenbeck ⓘ https://orcid.org/0000-0002-2825-3128

References

Andrews, M. D. 2001, SoPh, 204, 179
Bale, S. D., Goetz, K., Harvey, P. R., et al. 2016, SSRv, 204, 49
Bavassano-Cattaneo, M. B., Tsurutani, B. T., Smith, E. J., & Lin, R. P. 1986, JGR, 91, 11929
Belov, A., Papaioannou, A., Abunina, M., et al. 2021, ApJ, 908, 5
Brueckner, G. E., Howard, R. A., Koomen, M. J., et al. 1995, SoPh, 162, 357
Bruno, A., Christian, E. R., de Nolfo, G. A., Richardson, I. G., & Ryan, J. M. 2019, SpWea, 17, 419

Bryant, D. A., Cline, T. L., Desai, U. D., & McDonald, F. B. 1962, JGR, 67, 4983

Cane, H. V., & Lario, D. 2006, SSRv, 123, 45

Cane, H. V., Richardson, I. G., & Wibberenz, G. 1995, in Proc. 24th Int. Cosmic Ray Conf., Vol 4, ed. N. Lucci & E. Lamanna (London: International Union of Pure and Applied Physics), 377

Cane, H. V., Richardson, I. G., & von Rosenvinge, T. T. 1993, JGR, 98, 13295

Case, A. W., Kasper, J. C., Stevens, M. L., et al. 2020, ApJS, 246, 43

Chi, Y., Shen, C., Wang, Y., et al. 2016, SoPh, 291, 2419

Chitta, L. P., Priest, E. R., & Cheng, X. 2021, ApJ, 911, 133

Cohen, C. M. S., Christian, E. R., Cummings, A. C., et al. 2021, A&A, submitted

Desai, M., Dayeh, M., Smith, C., Mason, G., & Lee, M. 2012, in AIP Conf. Ser., 1436, Physics of the Heliosphere: A 10 Year Retrospective, ed. J. Heerikhuisen, G. Li, N. Pogorelov, & G. Zank (Melville, NY: AIP), 110

Domingo, V., Fleck, B., & Poland, A. I. 1995, SoPh, 162, 1

Ellison, D. C., & Ramaty, R. 1985, ApJ, 298, 400

Fox, N. J., Velli, M. C., Bale, S. D., et al. 2016, SSRv, 204, 7

Giacalone, J. 2012, ApJ, 761, 28

Giacalone, J. 2015, ApJ, 799, 80

Giacalone, J., Burgess, D., Bale, S. D., et al. 2021, ApJ, submitted

Gold, R. E., Krimigis, S. M., Hawkins, S. E., I., et al. 1998, SSRv, 86, 541

Gordon, B. E., Lee, M. A., Möbius, E., & Trattner, K. J. 1999, JGR, 104, 28263

Gosling, J. T., Baker, D. N., Bame, S. J., et al. 1987, JGR, 92, 8519

Guo, Y., Thompson, P., Wirzburger, J., et al. 2021, AcAau, 179, 425

Hill, M. E., Mitchell, D. G., Andrews, G. B., et al. 2017, JGRA, 122, 1513

Howard, R. A., & Vourlidas, A. 2018, SoPh, 293, 55

Hundhausen, A. J. 1972, Coronal Expansion and Solar Wind (Berlin: Springer)

Janvier, M., Dasso, S., Démoulin, P., Masías-Meza, J. J., & Lugaz, N. 2015, JGRA, 120, 3328

Kaiser, M. L., Kucera, T. A., Davila, J. M., et al. 2008, SSRv, 136, 5

Kahler, S. W., & Reames, D. V. 1991, JGR, 96, 9419

Kahler, S. W., Sheeley, N. R., J., Howard, R. A., et al. 1984, JGR, 89, 9683

Kasper, J. C., Abiad, R., Austin, G., et al. 2016, SSRv, 204, 131

Kataoka, R., Watari, S., Shimada, N., Shimazu, H., & Marubashi, K. 2005, GeoRL, 32, L12103

Kennel, C. F., Coroniti, F. V., Scarf, F. L., et al. 1986, JGR, 91, 11917

Kilpua, E., Koskinen, H. E. J., & Pulkkinen, T. I. 2017, LRSP, 14, 5

Kilpua, E. K. J., Good, S. W., Ala-Lahti, M., et al. 2021, FrASS, 7, 109

Kollhoff, A., Kouloumvakos, A., Lario, D., Dresing, N., et al. 2021, A&A, in press

Laitinen, T., & Dalla, S. 2021, ApJ, 906, 9

Lario, D., Berger, L., Decker, R. B., et al. 2019, AJ, 158, 12

Lario, D., & Decker, R. B. 2002, GeoRL, 29, 1393

Lario, D., Decker, R. B., Ho, G. C., et al. 2005, in AIP Conf. Ser., 781, The Physics of Collisionless Shocks: 4th Annual IGPP Int. Astrophysics Conf., ed. G. Li, G. P. Zank, & C. T. Russell (Melville, NY: AIP), 180

Lario, D., Decker, R. B., Roelof, E. C., & Viñas, A. F. 2015a, ApJ, 813, 85

Lario, D., Decker, R. B., Roelof, E. C., & Viñas, A. F. 2015b, JPhCS, 642, 012014

Lario, D., Ho, G. C., Decker, R. B., et al. 2003, in AIP Conf. Ser., 679, Solar Wind Ten, ed. M. Velli et al. (Melville, NY: AIP), 640

Lee, M. 1983, JGRA, 88, 6109

Lee, M. a. 2005, ApJS, 158, 38

Lee, M. A. 2006, GMS, 165, 245

Lepping, R. P., Berdichevsky, D. B., Burlaga, L. F., et al. 2001, SoPh, 204, 285

Li, G., & Lugaz, N. 2020, ApJ, 905, 8

Lin, R. P., Anderson, K. A., Ashford, S., et al. 1995, SSRv, 71, 125

Liu, Y., Richardson, J. D., Belcher, J. W., Kasper, J. C., & Skoug, R. M. 2006, JGRA, 111, A09108

Liu, Y. D., Luhmann, J. G., Kajdič, P., et al. 2014, NatCo, 5, 3481

Lugaz, N., Farrugia, C. J., Smith, C. W., & Paulson, K. 2015, JGRA, 120, 2409

Lugaz, N., Farrugia, C. J., Winslow, R. M., et al. 2018, ApJL, 864, L7

Lugaz, N., Temmer, M., Wang, Y., & Farrugia, C. J. 2017, SoPh, 292, 64

Mäkelä, P., Gopalswamy, N., Akiyama, S., Xie, H., & Yashiro, S. 2011, JGRA, 116, A08101

Marhavilas, P. K., Malandraki, O. E., & Anagnostopoulos, G. C. 2015, P&SS, 117, 192

McComas, D. J., Alexander, N., Angold, N., et al. 2016, SSRv, 204, 187

McComas, D. J., Bame, S. J., Barker, P., et al. 1998, SSRv, 86, 563

Moissard, C., Fontaine, D., & Savoini, P. 2019, JGRA, 124, 8208

Moncuquet, M., Meyer-Vernet, N., Issautier, K., et al. 2020, ApJS, 246, 44

Müller-Mellin, R., Kunow, H., Fleißner, V., et al. 1995, SoPh, 162, 483

Neugebauer, M., & Goldstein, R. 1997, GMS, 99, 245

Ogilvie, K. W., Chornay, D. J., Fritzenreiter, R. J., et al. 1995, SSRv, 71, 55

Palmerio, E., Kilpua, E. K. J., & Savani, N. P. 2016, AnGeo, 34, 313

Richardson, I. G. 1997, GMS, 99, 189

Richardson, I. G., & Cane, H. V. 1996, JGR, 101, 27521

Richardson, I. G., & Cane, H. V. 2010a, SoPh, 264, 189

Richardson, I. G., & Cane, H. V. 2010b, JGRA, 115, A07103

Richardson, I. G., & Cane, H. V. 2011, SoPh, 270, 609

Roelof, E. C., Krimigis, S. M., Mitchell, D. G., et al. 2010, in AIP Conf. Ser., 1302, Pickup Ions Throughout the Heliosphere and Beyond, ed. J. Le Roux et al. (Melville, NY: AIP), 133

Russell, C. T., Mewaldt, R. A., Luhmann, J. G., et al. 2013, ApJ, 770, 38

Salman, T. M., Lugaz, N., Farrugia, C. J., et al. 2020, ApJ, 904, 177

Sanderson, T. R., Beeck, J., Marsden, R. G., et al. 1990, GMS, 58, 385

Sanderson, T. R., Erdös, G., Balogh, A., et al. 2000, JGR, 105, 18275

Sanderson, T. R., Reinhard, R., van Nes, P., & Wenzel, K. P. 1985, JGR, 90, 19

Sauer, H. H. 1993, in Proc. 23rd Int. Cosmic Ray Conf. Vol. 3, ed. D. A. Leahy, R. B. Hicks, & D. Venkatesan (Singapore: World Scientific), 250

Shaikh, Z. I., Raghav, A. N., Vichare, G., Bhaskar, A., & Mishra, W. 2018, ApJ, 866, 118

Shen, C., Wang, Y., Ye, P., & Wang, S. 2008, SoPh, 252, 409

Sibeck, D. G., Decker, R. B., Mitchell, D. G., et al. 2001, JGR, 106, 21675

Sibeck, D. G., Phan, T. D., Lin, R., Lepping, R. P., & Szabo, A. 2002, JGRA, 107, 1271

Siscoe, G., & Odstrcil, D. 2008, JGRA, 113, A00B07

Skoug, R. M., Gosling, J. T., Steinberg, J. T., et al. 2004, JGRA, 109, A09102

Smart, D. F., & Shea, M. A. 1996, AdSpR, 17, 113

Smith, C. W., L'Heureux, J., Ness, N. F., et al. 1998, SSRv, 86, 613

Smith, C. W., Ness, N. F., Burlaga, L. F., et al. 2001, SoPh, 204, 227

Temmer, M., Holzknecht, L., Dumbović, M., et al. 2021, JGRA, 126, e28380

Torsti, J., Riihonen, E., & Kocharov, L. 2004, ApJL, 600, L83

van Nes, P., Reinhard, R., Sanderson, T. R., Wenzel, K. P., & Zwickl, R. D. 1984, JGR, 89, 2122

Wiedenbeck, M. E., Angold, N. G., Birdwell, B., et al. 2017, in 35th Int. Cosmic Ray Conf., Proceedings of Science Vol. 301, 16, https://pos.sissa.it/cgi-bin/reader/conf.cgi?confid=301

Wilson, L. B., Chen, I., Wang, S., et al. 2019a, ApJS, 243, 8

Wilson, L. B., Chen, I., Wang, S., et al. 2019b, ApJS, 245, 24

Wilson, L. B., Chen, I., Wang, S., et al. 2020, ApJ, 893, 22

Wuelser, J.-P., Lemen, J. R., Tarbell, T. D., et al. 2004, Proc. SPIE, 5171, 111

Xu, M., Shen, C., Chi, Y., et al. 2019, ApJ, 885, 54

Yashiro, S., Gopalswamy, N., Michalek, G., et al. 2004, JGRA, 109, A07105

Zhao, L. L., Zank, G. P., Khabarova, O., et al. 2018, ApJL, 864, L34

Zurbuchen, T. H., & Richardson, I. G. 2006, SSRv, 123, 31